instruments

MDPI

Article

Analysis of Near-Field Magnetic Responses on $ZrTe_5$ through Cryogenic Magneto-THz Nano-Imaging

Samuel Haeuser [1,2], Richard H. J. Kim [2], Joong-Mok Park [2], Randall K. Chan [1,2], Muhammad Imran [2], Thomas Koschny [1,2] and Jigang Wang [1,2,*]

[1] Department of Physics and Astronomy, Iowa State University, Ames, IA 50011, USA; rkchan@iastate.edu (R.K.C.)
[2] Ames National Laboratory, Ames, IA 50011, USA; rkim@iastate.edu (R.H.J.K.); imran@iastate.edu (M.I.)
* Correspondence: jgwang@iastate.edu

Abstract: One manifestation of light-Weyl fermion interaction is the emergence of chiral magnetic effects under magnetic fields. Probing real space magnetic responses at terahertz (THz) scales is challenging but highly desired, as the local responses are less affected by the topologically trivial inhomogeneity that is ubiquitous in spatially averaged measurements. Here, we implement a cryogenic THz microscopy instrument under a magnetic field environment—a task only recently achieved. We explore the technical approach of this system and characterize the magnetic field's influence on our AFM operation by statistical noise analysis. We find evidence for local near-field spatial variations in the topological semimetal $ZrTe_5$ up to a 5-Tesla magnetic field and obtain near-field THz spectra to discuss their implications for future studies on the chiral magnetic effect.

Keywords: near-field; scanning near-field optical microscope (SNOM); THz-SNOM; cryogenic; magnetic

Citation: Haeuser, S.J.; Kim, R.H.J.; Park, J.M.; Chan, R.K.; Imran, M.; Koschny, T.; Wang, J. Analysis of Near-Field Magnetic Responses on $ZrTe_5$ through Cryogenic Magneto-THz Nano-Imaging. *Instruments* **2024**, *8*, 21. https://doi.org/10.3390/instruments8010021

Academic Editor: Pasquale Arpaia

Received: 9 January 2024
Revised: 19 February 2024
Accepted: 25 February 2024
Published: 5 March 2024

1. Introduction

The terahertz (THz) spectral region proves to be ideal in exploring the collective modes [1] and robust transport phenomena [2,3] inherent in quantum and topological materials. Despite compelling evidence of dynamical chiral magnetic effects (d-CMEs) in magnetotransport/optical measurements of topological semimetals, there are two key outstanding issues. First, the ensemble-averaged measurements used so far cannot resolve or eliminate the ubiquitous nano-/micro-scale electronic inhomogeneity, e.g, magnetic-field- or electric-contact-induced heterogeneous current flows [4,5]. Second, d-CMEs have only been shown from either electronic [6,7] or lattice subsystems [8]. Thus far, there has been a lack of probes to underpin their real space signatures. One fundamental challenge in probing and understanding the dynamical chiral magnetic phenomena is the need for "nano-THz" instrumentation [9–22] capable of viewing local magneto-THz spectra while operating simultaneously at high Tesla magnetic fields and liquid-helium temperatures. Another challenge comes the development of THz sources and detectors capable of accessing a broadband THz range [23,24]. In recent years, there have been many systems that have enabled progress towards this goal [25–30], including a recent study utilizing high magnetic fields at infrared frequencies [31]; however, such a nano-THz microscope under these conditions has only recently been achieved [32].

Our cryogenic magneto-terahertz scattering-type near-field optical microscope system (cm-THz-sSNOM) is a microscopy machine that allows the simultaneous non-contact probing of nanoscale spatial variations and nanoscale THz spectra while operating under extreme conditions of liquid-helium temperatures and high magnetic fields. Shown in Figure 1a is a representation of the THz probe above the THz near-field response of zirconium pentatelluride ($ZrTe_5$) operating at 5 T magnetic fields and 58 K. In this geometry, THz light (red line) is focused on a sharp metal tip acting as an antenna, which induces oscillatory

polarization charges perpendicular to the surface and concentrates the electric field within local near-field interactions on the order of the tip apex size. Notably, this THz near-field scheme provides two strategic advantages: first, it allows the determination of local responses that can be masked by topologically trivial artifacts from sample inhomogeneity due to electric contact, impurities and strain; second, it measures these features along the vertical direction (perpendicular to the sample plane), which is normally very difficult to access by far-field optical and transport measurements.

We developed and applied a versatile THz nanoscope and applied it to a unique Dirac material suitable for the study of local magnetic coherence and dynamics, zirconium pentatelluride ($ZrTe_5$). $ZrTe_5$ hosts multiple phases of topological insulators (TIs) and Dirac and Weyl semimetals (DSM/WSM) [33–36], which support magnetic-field-, light-, strain- and temperature-induced topological phase transitions [37–39]. Recently, an ambient condition, non-magnetic THz-SNOM, has been used to reveal the complex spatial heterogeneity in $ZrTe_5$ [19]. The cm-THz-sSNOM advances the state of art to probe magnetic-field-induced phenomena below liquid-helium temperatures at simultaneous "THz-nano" scales, not accessible in any study of topological matter until our recent work.

In this work, we applied our cm-THz-sSNOM to study the operation conditions and parameters in $ZrTe_5$ to provide insights into its base performance, noise characteristics and nano-THz techniques. The measured nano-magneto-THz spectra along the out-of-plane field direction show field-induced spatial and spectral variations. Our approach aims to push the state of the art to eventually unambiguously resolve the deep-subwavelength spatial variations that are influenced by the nanoscale topological edge transport. This entry marks significant progress in visualizing these effects by obtaining the genuine magnetic features exclusive to homogeneous, nanometer regions.

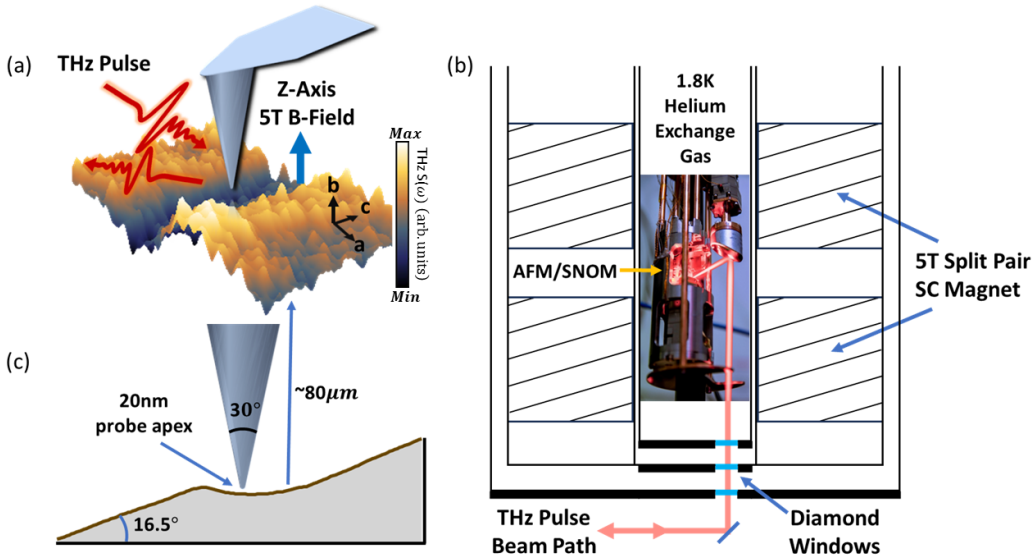

Figure 1. (**a**) Representative diagram of Rocky Mountain Nanotechnology LLC atomic force microscope (AFM) probe above a the scattered THz signal S_1 operating at 5 T and 58 K, which shows the crystal axis orientation for $ZrTe_5$. The 5 T magnetic field is perpendicular to the sample surface (z direction). (**b**) Cryogenic–magnetic SNOM operational setup consisting of a low-temperature wet cryostat utilizing a 1.8 K helium exchange gas, a 5 T split-pair superconducting magnet, 3 diamond windows and an AFM. The THz light utilizes the same parabolic mirror to focus and collect the scattered light. (**c**) The scaling of the geometry of the sample topography under the AFM probe. The Rocky mountain probe is an 80-um-long solid platinum probe with a tip apex of 20 nm. The sample is initially tilted by 16.5 degrees for all scans.

2. Materials and Methods

Our custom-made cm-THz-sSNOM is based on a tapping-mode atomic force microscope (AFM) excited by ultrashort THz pulses inside a top-loading 5-Tesla split-pair magnet cryostat with a base temperature of 1.8 K. The AFM metallic probe acts as an antenna that receives far-field THz pulses, amplifies the near-field interaction through the enhancement of the THz field by tip resonances and finally transmits and scatters the THz near-field to the far field for electro-optical (EO) sampling [32].

The instrument comprises three main components: a laser, a cryostat and an AFM unit. The laser is a femtosecond ytterbium laser with pulse energy of 3 µJ, a repetition rate of 1 MHz and a central laser wavelength of 1045 nm that can generate an intense source of pulsed THz radiation when applied to a OH1 nonlinear organic THz-emitting crystal. The cryostat is a wet, top-loading, 5-Tesla split-pair superconducting coil magnet cryostat with a base temperature of 1.7 K. This can operate in a wide range of temperatures from 1.8 K to 300 K, as well as any magnetic field up to 5 T simultaneously. The AFM is a fiber-based cantilever AFM system from Attocube Systems designed for applications at low temperatures and in high magnetic fields. As shown in Figure 1b, the AFM is designed to sit centrally inside this split-pair magnet to provide a uniform magnetic field perpendicular to the sample surface. Both positive and negative fields can be applied by varying the current in the superconducting magnet. This magnet may also operate in a persistent mode, requiring no external current to maintain a constant field strength suitable for long scans and stability. The cryostat is equipped with 3 diamond windows with transmission efficiency of 70% for each window. The total THz electric field scattered from the tip is attenuated to $\sim 1/3$ by the windows before reaching our detection system. The THz near-field signal is detected by utilizing a CdTe-based electro-optic (EO) sampling scheme.

The AFM probe responsible for accepting THz and scattering the near-field responses is a solid platinum-wire-based probe produced by Rocky Mountain Nanotechnology, LLC model 25Pt300B, as shown to scale above the unaltered $ZrTe_5$ topography in Figure 1c. This choice of solid platinum probe has been utilized in many THz near-field systems and they have shown stable operation under conditions such as high-temperature, low-temperatures and a variety of room-temperature experiments [9,14,40–42]. This probe is 80-µm-long and has a nominal apex radius of 20 nm and a tapping frequency of 20 KHz. Well-documented studies on THz probes show this geometry to be near-optimal while retaining a sub-20 nm resolution [43]. The probe is illuminated by a THz pulse with an incident angle of 60°.

Once the probe is in contact with the sample, near-field signals are extracted from the scattered THz signal by demodulating the backscattered radiation collected from the tip–sample system at the n-th harmonics of the tip-tapping frequency of the AFM (n = 1 or 2). Time-domain THz spectroscopy can be performed by moving the motorized stage that controls the time delay of the optical sampling pulse to the electro-optic crystal to trace out the electric field waveform of the scattered THz near-field amplitude in the time domain. To obtain near-field images, the sample stage underneath the tip is raster-scanned while the THz sampling delay is fixed to a position that gives the largest near-field amplitude. Under this raster scanning process, the tip is moved across the same topographic features in both the forward (left to right) and backward (right to left) directions, generating two independent images. It should be noted that the probe will respond slightly differently in each direction as the movement sees a falling action in one direction and a rising action in the opposing direction for a given topographic feature; however, with slow scan speeds, the results are expected to be qualitatively similar with a small margin of error. Nano-spectroscopy is achieved by scanning the sampling delay to directly trace out the oscillating THz electric field waveforms in the time domain while the tip is positioned at a fixed location on the sample.

3. Results and Analysis

We use the cm-THz-sSNOM to study a single-crystal $ZrTe_5$ sample that exhibits 3D linear dispersion. The sample was grown by the flux growth method and its basic properties

were characterized by using magneto-transport, angle-resolved photoemission, Raman and other extensive chemical, structural and optical characterizations [3,33].

Images for $ZrTe_5$ were taken at 58 K under varying magnetic fields to tune the Fermi surface to the Lifshitz transition point, as noted in other works for this sample [3,33]. Figure 1c shows, to scale, the $ZrTe_5$ topography under the AFM probe through a line cut of the raster scan images at 58 K and a 5 T magnetic field. The sample has an unintentional consistent tilt of 16.5° to the expected topography due to an uneven layer of adhesive when mounting the sample. All the AFM topography images further have been corrected for the same global tilt parameter to the assumed topography, revealing a step-like structure in the sample surface.

3.1. Methods of Analyzing Topography

The forward scanning topography for 0 T, 0.3 T, 1.5 T and 5 T is shown in Figure 2a, 2b, 2c and 2d, respectively.

Several clear key features are able to be resolved under all magnetic field scans. The first is a circular "mound" approximately 2 µm in diameter and 40 nm high. The second is a large, 1.5-µm-wide, 600-nm-high step spanning the length of the image. Furthermore, there are several small topographic features consistent under each magnetic field, such as a well-defined 20 nm trench at the bottom of this large step. We use these images as the basis when implementing new techniques to visualize fine features and characterize the magnetic field's effects on our AFM's performance.

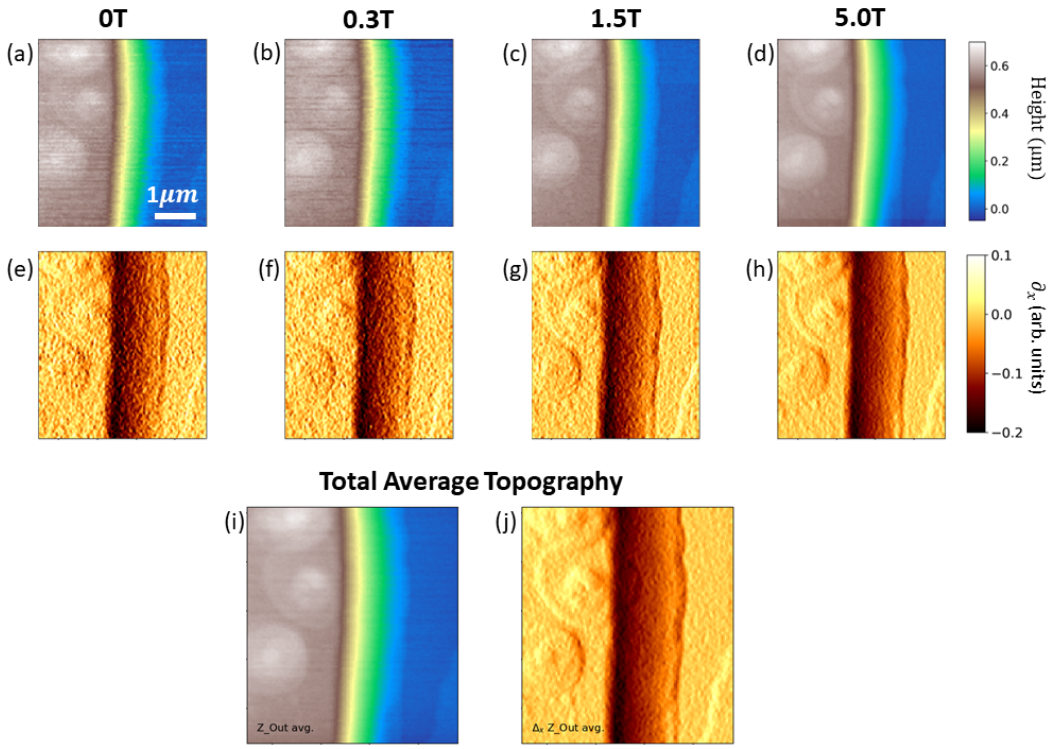

Figure 2. (**a**) AFM topographic profile for $ZrTe_5$ taken at 58 K and (**a**) 0 T, (**b**) 0.3 T, (**c**) 1.5 T and (**d**) 5.0 T. Corresponding Sobel gradient of (**e**) 0 T, (**f**) 0.3 T, (**g**) 1.5 T and (**h**) 5 T topography. (**i**) Averaged AFM topography after correlation. (**j**) Averaged Sobel gradient topography after correlation.

3.1.1. Detecting Fine Features and Edges Hidden by Large Topographic Variations—Sobel Operator

In order to perform an accurate analysis while not neglecting the wide variance in the topographic features, we applied a first-order gradient in the tip scanning direction (horizontal). To address the possible point-by-point variation caused by the discrete possible readout of the Z-piezo scanner, we implemented the Sobel operator [44].

The Sobel operator is a widely used algorithmic gradient and filter used in digital image processing and edge detection [45]. The operation is defined by a convolution between the AFM topography and the kernel $G_x = \begin{bmatrix} -1 & 0 & 1 \\ -2 & 0 & 2 \\ -1 & 0 & 1 \end{bmatrix}$, with each of the raw topographic images for different magnetic fields able to reveal the gradient in the x direction.

The resulting images after applying the horizontal Sobel operator are shown in Figure 2e–h, for the corresponding magnetic field topographies detailed above. There are several benefits of using such an operator in this case. First, the gradient removes any global tilt for both the x and y directions caused by an uneven sample surface when mounting. In addition, this highlights areas of constant slope (i.e., similarly sloped regions of the sample are colored similarly) to give insights into the expected true topography. In our case, this shows two similarly sloped regions on the sides connected by a varying slope region in the center of the images. This leads us to conclude that the global offset the we applied earlier is reasonable. Second, this clearly highlights key details of the surface otherwise hidden by larger features. Since the topography in AFM can sometimes span several micrometers in height, many fine nanometer features can become hidden by large hills, bumps, valleys, etc. Finally, since the gradient operator relies on the sharpness of the edge rather than the overall height, this can be used for more exact cross-correlations of the topographic features.

One may also apply a Sobel operator against the tip scanning direction to reveal edges sensitive to the y direction only; however, this may require additional analysis due to the typical line-by-line height variation seen commonly in AFM images. The operator can be defined by a convolution of the topography with a symmetric kernel given by $G_y = \begin{bmatrix} -1 & -2 & -1 \\ 0 & 0 & 0 \\ 1 & 2 & 1 \end{bmatrix}$. We find little benefit in our case compared to applying the operator in the tip scanning direction.

3.1.2. Correlating Topography under Different Conditions and "Noise-Free" Reference

Utilizing the Sobel operator allows us to perform a statistical cross-correlation to a high degree of accuracy in order to align the spatial coordinates of successive scans of the sample to one another. We first pick one scan at random (0.3 T forward trace) and generate a cross-correlation map between each of the other 7 scans recorded (see Appendix A for cross-correlation quantities). This allows us to find x–y translation vectors to apply to each of the images. We also have the benefit of using the same translation vectors for the SNOM data discussed later. We have applied these translations to each trace in the study for consistency.

Under the assumption that the topographic features that the AFM records do not change in time or under an applied magnetic field, we can now average all 8 AFM images to produce an unfiltered "noise-free" version of the AFM topography for study. Figure 2i,j show the 8× averaged AFM topography for the real space height and gradient, respectively.

3.1.3. Statistically Quantifying Magnetic Field Effects on AFM Operation

We take the 8× averages of all the topographic data for this sample (4× B-field, forward and backwards) as the lowest possible noise comparison to each of the individual conditions described above. By subtracting an individual topography from the average topography, we can generate a spatial noise distribution/variance plot. Figure 3a,b show the spatial distribution of noise for the 0 T and 5 T real space topography under the extreme cases in a global color scale. We find that the reduction in variation from the average scales with higher magnetic fields with 5 T showing the cleanest overall AFM scans for the entire experiment, followed by the 1.5 T, 0.3 T and finally 0 T magnetic fields. Interestingly, the AFM performance becomes less noisy under a magnetic field. We believe that this is an artifact caused by eddy currents induced on the solid metallic probe during its tapping

motion under the magnetic field, causing dampening and possible noise reduction. During operation, this dampening effect was observed and its effect on the tapping amplitude was mitigated by applying a higher tapping excitation to bring the system to the same nominal tapping amplitude for each scan, but the noise reduction remained.

Figure 3c,d show the spatial Fourier transform of the corresponding noise plots of 0 T and 5 T, respectively. Here, kx describes the spatial frequency along the tip scanning direction, while ky describes the spatial frequency against the tip scanning direction. The brighter color scale describes larger variations at a given frequency in kx and ky. The strong response along kx = 0 depicts the explicit line-by-line variation seen in the spatial noise map. Another important feature is the minimal high-frequency "point-by-point" variation seen in all large kx and ky. Finally, and possibly most importantly in understanding the tip response and influence on future SNOM scans, the overall noise shown in all magnetic fields is similar. While the overall amplitude of the noise decreases, the type of noise and therefore the cause of the noise remains unchanged. In other words, the only observed influence of the magnetic field on the AFM performance is a change in some multiplicative factor of the noise. By comparing the noise spectral power density calculated by the RMS noise plots between 0 T and 5 T (see Appendix A), we find the multiplicative factor in the the reduction of the noise to be 1.84. We conclude that the AFM sees the same response from topographic features under all magnetic field conditions with a variation in the amount of noise in the final image.

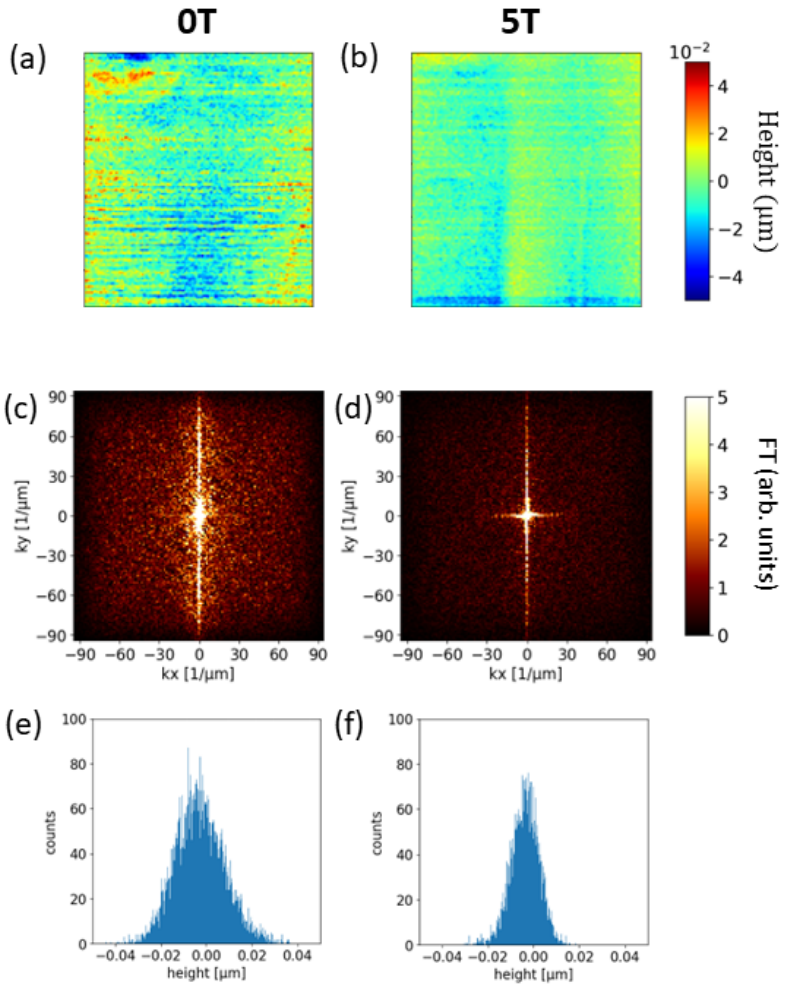

Figure 3. AFM forward scan noise plot generated by subtracting the total spatial average for (**a**) 0 T and (**b**) 5 T. Fourier transform of corresponding (**c**) 0 T and (**d**) 5 T noise plots. Histograms of corresponding (**e**) 0 T and (**f**) 5 T noise plots.

We also investigate histograms for the distribution of variation from the 8× average scan. This is plotted in Figure 3e,f for the respective 0 T and 5 T analysis above. This visualization clearly shows a reduction in the noise amplitude under magnetic fields. This reduction leads to the broadening of the distribution, although the distribution itself remains qualitatively unchanged. We also perform the same complete analysis presented here on the horizontal gradient average as a method to describe the noise (see Appendix A). We find the same conclusions as discussed for the real space topography; however, as this removes the line-by-line variations and the global sample tilt inherent to the scanning motion, we see a simple constant blanket of noise. This furthers supports our conclusion that the influence of the magnetic field changes some multiplicative factor of the noise without affecting any AFM resolution or response.

3.2. Deep Sub-Wavelength THz Near-Field imaging

The THz near-field signal was collected simultaneously for each magnetic field described above. As noted in our previous studies [19,21,22,32], the decay distance for the THz s_1 signal can be more than a thousand times shorter than the free-space THz wavelength. The THz-generating OH1 organic crystal in this demonstration was mounted to a substrate not suitable for the heat generated by the pump laser and caused damage for long exposure times. This led to the slow decay of the THz near-field signals during the scanning process. Mounting the crystal to a window that was a more suitable thermal conductor fully remedied this for future experiments. Thus, in these tests, to balance the signal-to-noise constraints of s_2 during this particular operation and crystal exposure time, we chose to use the higher s_1 harmonic to analyze the near-field spatial features.

We use the previous method of cross-correlating the AFM topography and provide a global shift parameter to each of the SNOM images. This allows the averaging of the forward and backward trace to improve the signal to noise and reduce the bias of choice when presenting the images. Since this slightly filters the tip response crossing the topographic boundary, the final averaged SNOM image shows less sharp edge transitions in favor of an overall cleaner image. The first harmonic s_1 images taken at 58 K are plotted for 0 T, 0.3 T, 1.5 T and 5 T in Figure 4a, 4b, 4c, and 4d, respectively, under a global color scale by reference of the absolute signal amplitude.

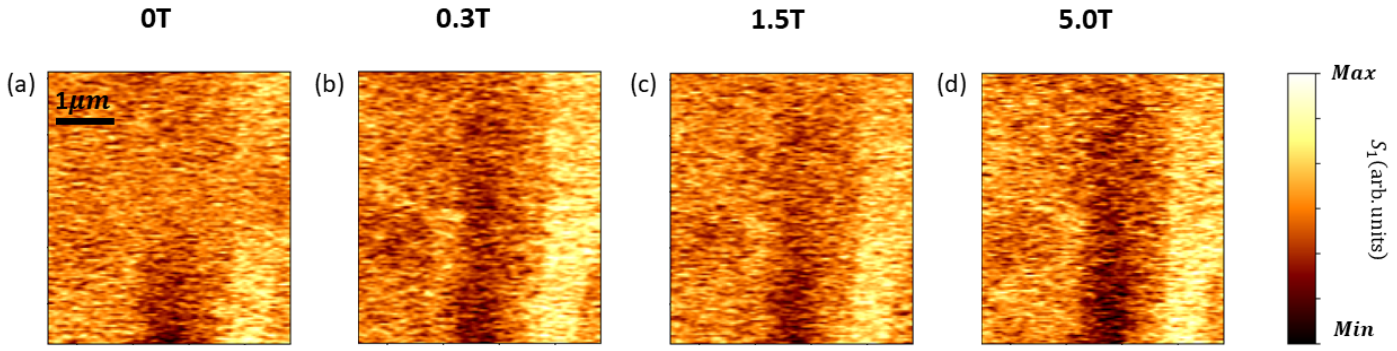

Figure 4. Forward and backward averaged THz s_1 near-field images taken at 58 K and (**a**) 0 T, (**b**) 0.3 T, (**c**) 1.5 T and (**d**) 5.0 T under a global color scale.

As mentioned above, each scan experiences a slow decay in the THz signal in time, resulting in a reduction in contrast nearing the end of the scan frame. The 0 T image shows a fast decay to no signal and slight recovery by the end of the scan. We believe that this is caused by the phase shift between the sampling pulse and THz waveform from one peak to the next nearest peak. The 0 T trace has only been presented for the comprehensiveness of the study and should not be taken as a true representation of the sample contrast. All other images exhibit a predictable decay in the THz signal consistent with the deteriorating THz generation crystal.

We see clear contrasting features under all magnetic fields, seemingly related to the topographic locations revealed in the gradient topography. Specifically, the upper plateau (left flat region) shows a striking contrast to that of the slight trench within the lower plateau. Furthermore, the signal size outside of this trench in the lower plateau is similar to that of the higher plateau. Interestingly, we see a dark region when the tip is positioned along the ~1 μm, 600-nm-tall topographical slope between the two plateaued regions of the sample. The SNOM images also show contrast when probing over a ~2-μm-wide, 40-nm-tall "mound" seen in upper plateau of the topographic profile. The magnetic-field-induced changes are expected to be small in variation and thus further studies are required to obtain any detailed conclusions beyond this proof-of-concept work.

3.3. Deep Sub-Wavelength THz Time-Domain Spectroscopy

Time-domain THz spectroscopy was performed by tracing out the electric field waveform of the scattered THz near-field amplitude in time. We focus on two locations exhibiting a stark contrast in the lower plateau shown in the THz images above. We apply a fast Fourier transform (FFT) to the unmodified time trace to retrieve the corresponding THz near-field spectrum. The THz near-field spectrum in the bright strip region at 58 K for 0 T (black dashed), 0.3 T (red dashed) and 1.5 T (blue dashed) is shown in Figure 5a; the inset shows the corresponding time traces. The THz near-field spectrum outside the bright region at 58 K for 0 T (black solid), 0.3 T (red solid) and 1.5 T (blue solid) is shown in Figure 5b; the inset shows the corresponding time traces. The specific locations for these traces are shown in the inset of Figure 5c as a dashed circle and a solid circle, corresponding the dashed and solid data sets. We note that there are several dips in the spectrum that we attribute to tip resonances, water absorption and the complicated backscatter-style collection geometry used in the system. More specifically, we point out the spectral dips that appear, to some degree, at 0.57 THz, 0.93 THz, 1.35 THz and 1.75 THz.

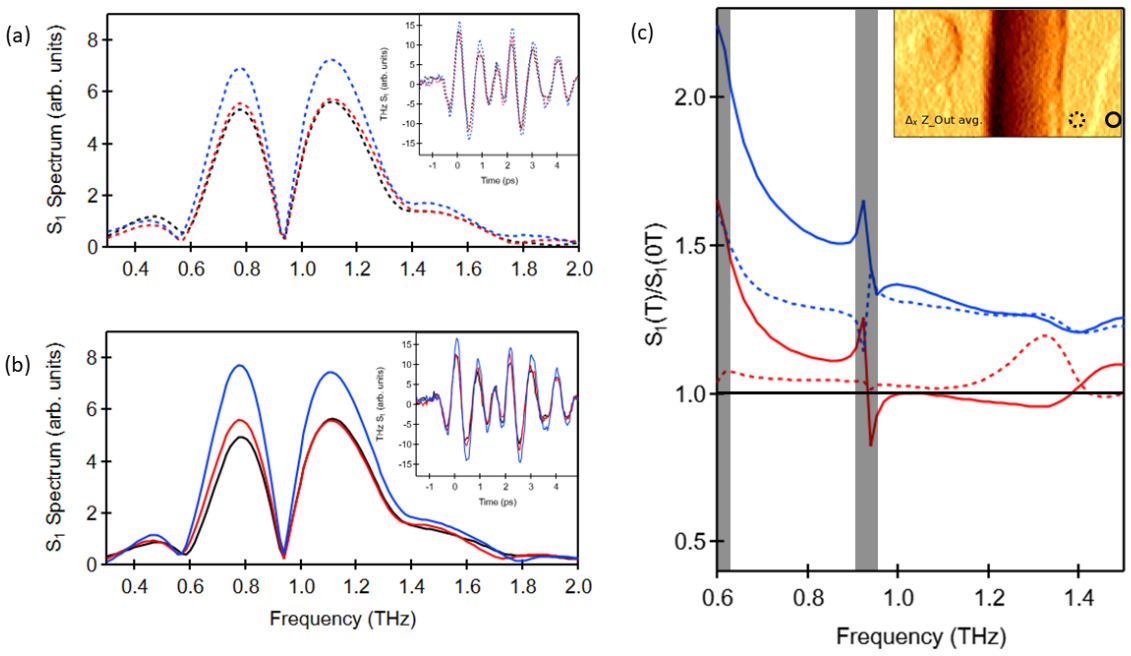

Figure 5. (**a**) Near-field spectrum at 58 K and various magnetic fields, 0 T (black dashed), 0.3 T (red dashed) 1.5 T (blue dashed), taken at dashed locations shown in inset of (**c**). Inset: corresponding time traces for dashed locations. (**b**) Spectrum at various magnetic fields, 0.0 T (black solid), 0.3 T (red solid) 1.5 T (blue solid), at solid locations shown in inset of (**c**). Inset: corresponding time traces for solid locations. (**c**) Spectral change referenced for 0.3 T (red) and 1.5 T (blue) to the 0 T trace for the corresponding dashed and solid locations in inset. The shaded locations cover spectral dips seen in (**a**,**b**). Inset: gradient topography and corresponding locations of interest.

Interestingly, the different locations show clear differences in the THz spectrum under magnetic fields. We explore this difference by using the ratio of each field's THz spectrum to the 0 T spectrum in its corresponding location. We plot this ratio in Figure 5c for the dashed and solid locations shown in the inset. We mark the near-zero spectral dips as gray shaded regions for clarity.

All locations exhibit a shift upward toward lower frequencies below 1 THz when applying high magnetic fields, while staying relatively flat above 1 THz but to varying degrees. Notably, applying a higher magnetic field for a given location (solid or dashed location) seems to show a stronger shift at lower frequencies. Surprisingly, the region showing a lower amplitude, matching that of the upper plateau in the THz images, shows the most extreme changes from the 0 T trace. Moreover, both locations under the same magnetic field (dashed and solid for a given magnetic field) show extraordinarily similar spectral responses above 1 THz while exhibiting quite different amounts of shifting below the 1 THz region.

4. Conclusions

In this study, we detail a newly developed cryogenic magneto-terahertz scattering-type near-field optical microscope system (cm-THz-sSNOM) and apply it to the topological material $ZrTe_5$ in order to demonstrate a detailed proof-of-concept operation by scanning and analysis. We show the system operating at magnetic fields up to 5 T and 58 K cryogenic temperatures by detailing the AFM performance, THz near-field images and THz nano-spectroscopy.

We detail the use of statistical methods to examine the AFM topography and noise characteristics to understand the possible impact of magnetic fields. We implement the Sobel operator as a gradient function to use in a cross-correlation algorithm to generate translation vectors. This serves as a great tool to visualize fine features, regardless of global shifts and large topographic changes. Using a noise-free reference picture, we generate noise statistics for the recorded topography. Importantly, the distribution of the noise remains similar under all magnetic fields; however, operating under magnetic fields generally leads to an overall reduction in noise. This leads us to the important conclusion that the AFM's resolution performance remains unchanged under changing magnetic fields.

Finally, we present THz near-field images and local THz spectra analysis to show a proof of concept of the system's operation. We find noticeable contrasts in the THz s_1 signal highly dependent on the topographical location. This may provide evidence enabling real space features to be explored and discussed elsewhere under a more detailed study outside the scope of this work. Furthermore, we provide near-field THz spectral data to show the consistent operational capabilities for time-domain spectroscopy under different magnetic field conditions. This reveals interesting spectral features also requiring further exploration and discussion outside the scope of this paper.

Author Contributions: R.H.J.K., J.-M.P. and S.H. performed the THz imaging measurements with J.W.'s supervision. S.H. and T.K. analyzed the data with the help of M.I. and R.K.C. The paper was written by S.H. with discussions with all authors. J.W. coordinated the project. All authors have read and agreed to the published version of the manuscript.

Funding: The modeling of magneto-THz nano-imaging was supported by the Ames National Laboratory, the US Department of Energy, Office of Science, Basic Energy Sciences, Materials Science and Engineering Division, under contract No. DEAC02-07CH11358. The THz sSNOM instrument was supported by the US Department of Energy, Office of Science, National Quantum Information Science Research Centers, Superconducting Quantum Materials and Systems Center (SQMS), under contract No. DE-AC02-07CH11359.

Data Availability Statement: The data that support the findings of this study are available from the corresponding author upon reasonable request.

Acknowledgments: We express our gratitude for the test samples provided by Q. Li and G. Gu.

Conflicts of Interest: The authors have no conflicts to disclose.

Appendix A

In this appendix, we present a brief description of the figures relevant to this paper in the context of the main text where noted.

Figure A1 shows the full cross-correlation used to find translation vectors in order to align all the topographic data in this study (4× B-fields and forward/backward scans). The 0.3 T forward scan is used as a reference to generate all other translations. From left to right: translation offset map, reference scan, input scan to be shifted and correlation mapping. Subsequent lines in the figure show the next scan to be correlated, as noted in the label for the input scan.

Figure A2 shows an example of the noise characteristic analysis of the forward scan described in the main text using the horizontal gradient. We take the 8× gradient average and, subtracting an individual gradient topography from the average, we can generate a spatial noise plot, FT and histogram that reiterate the random noise conclusion from the main text. It is important to note that as the gradient removes the pure vertical (y direction) variations, varying ky along kx = 0 will not yield any results, explaining the different shape in the FT plot.

We performed RMS analysis on the Sobel difference noise plots generated above. Figure A3 shows the RMS figures for both the forward and backward scanning directions. Using these plots, we generate a spectral power density, denoted Q, of each plot. Using these spectral power densities and a proxy for the amount of noise at each magnetic field, we can estimate the multiplicative factor of the noise reduction from the 0 T situation as 0.99 for 0.3 T, 1.29 for 1.5 T and 1.84 for 5 T.

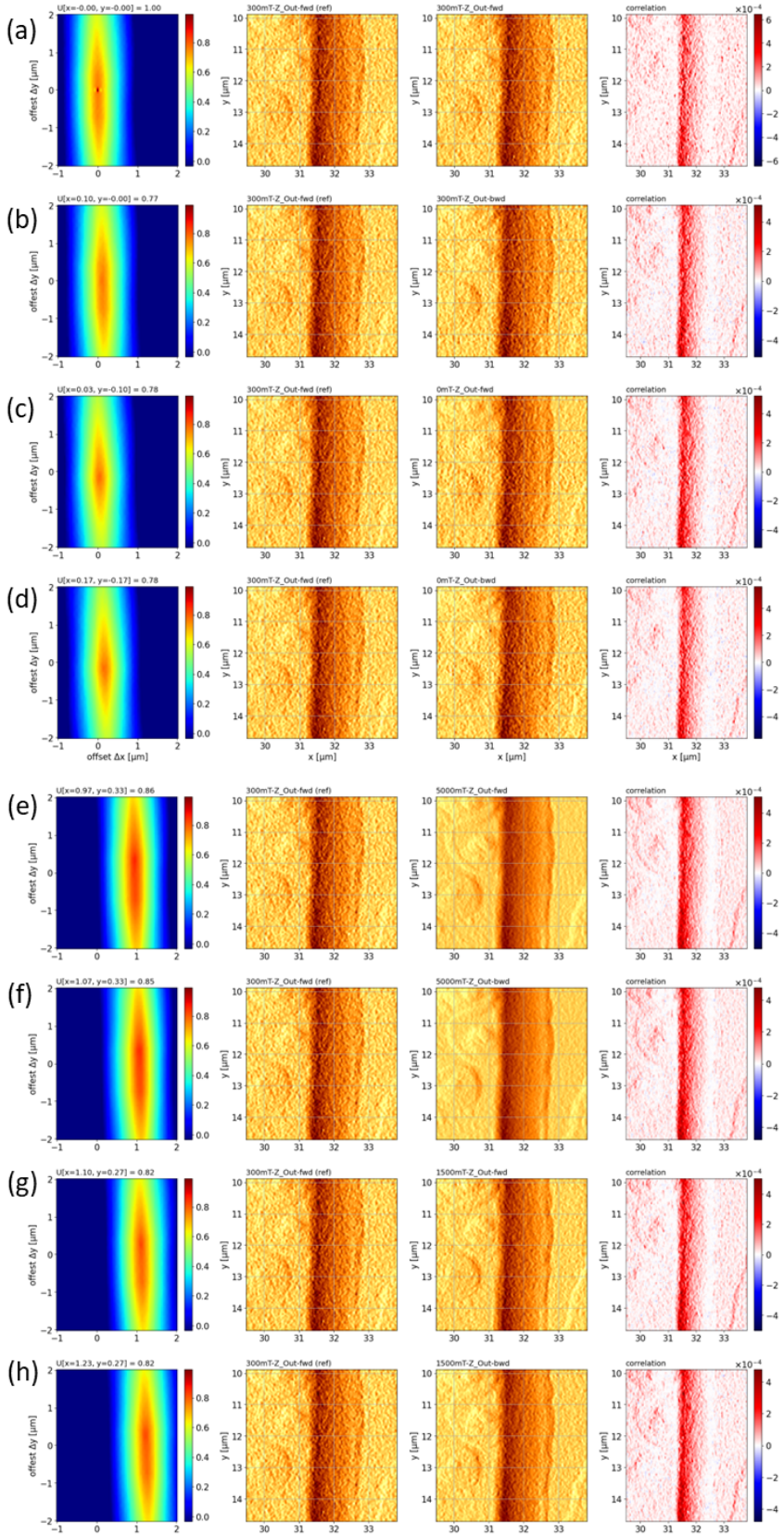

Figure A1. Cross-correlation statistics using the Sobel gradient for the translation vectors used in the main text, using the 0.3 T forward scanning plot as a translation reference for the (**a**) 0.3 T forward, (**b**) 0.3 T backward, (**c**) 0 T forward, (**d**) 0 T backward, (**e**) 5 T forward, (**f**) 5 T backward, (**g**) 1.5 T forward and (**h**) 1.5 T backward scans.

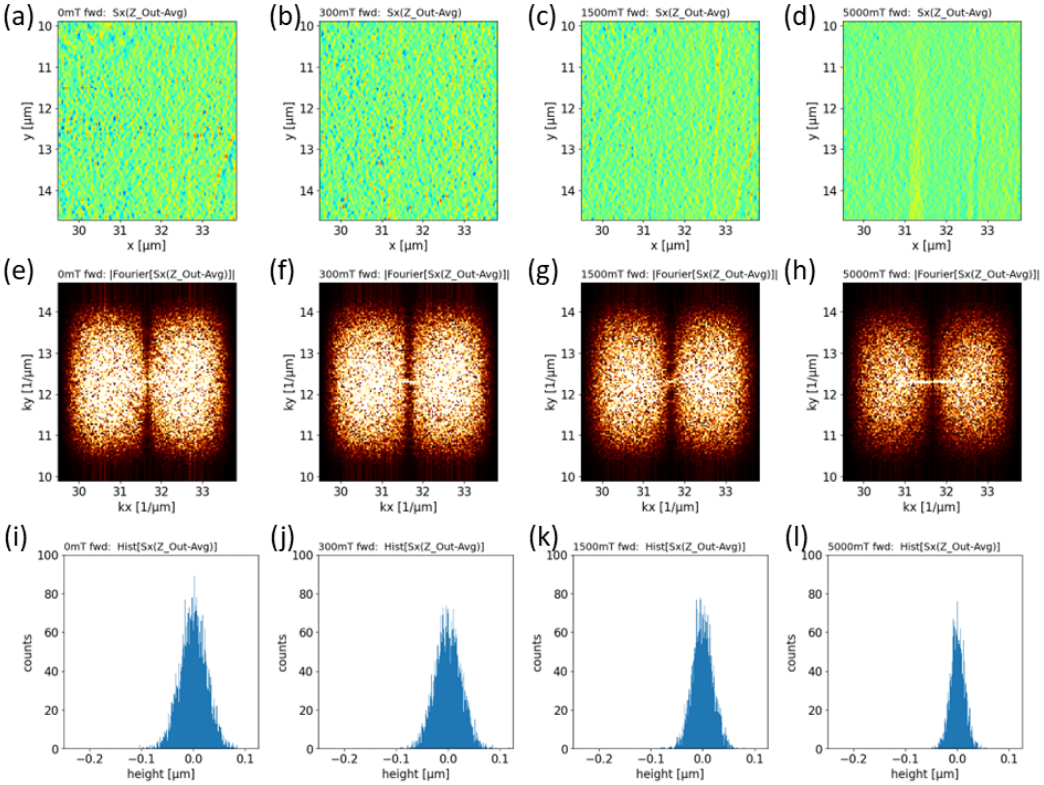

Figure A2. Statistical methods described in the main text applied to the Sobel gradient for the forward scanning direction. Noise plot generated by subtracting the total spatial average for (**a**) 0 T, (**b**) 0.3 T, (**c**) 1.5 T and (**d**) 5 T. Fourier transform of corresponding (**e**) 0 T, (**f**) 0.3 T, (**g**) 1.5 T and (**h**) 5 T noise plots. Histograms of corresponding (**i**) 0 T (**j**) 0.3 T, (**k**) 1.5 T and (**l**) 5 T noise plots.

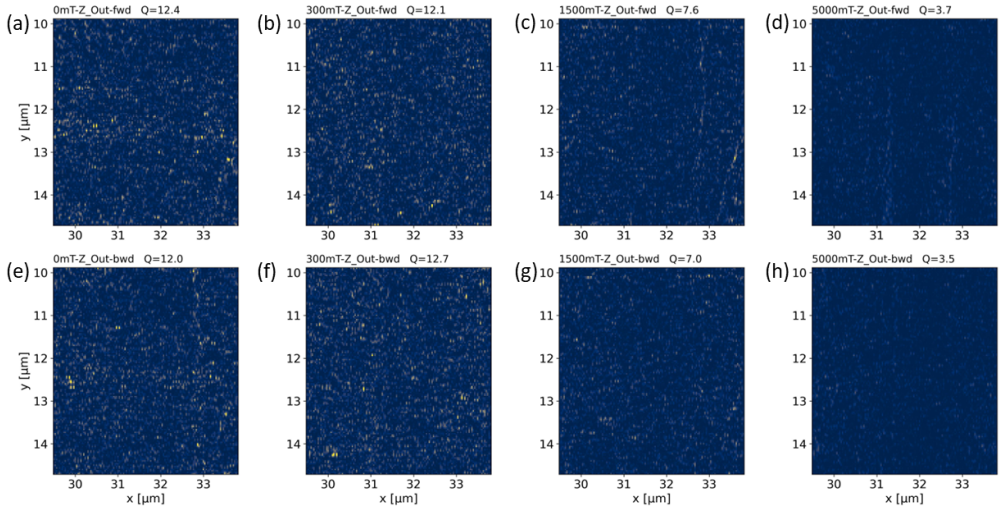

Figure A3. RMS difference noise plots in the forward scanning direction and corresponding spectral power densities denoted Q for (**a**) 0 T, (**b**) 0.3 T, (**c**) 1.5 T and (**d**) 5 T. Corresponding RMS difference noise plots in the backward scanning direction for (**e**) 0 T, (**f**) 0.3 T, (**g**) 1.5 T and (**h**) 5 T.

References

1. Luo, L.; Mootz, M.; Kang, J.H.; Huang, C.; Eom, K.; Lee, J.W.; Vaswani, C.; Collantes, Y.G.; Hellstrom, E.E.; Perakis, I.E.; et al. Quantum Coherence Tomography of Light–Controlled Superconductivity. *Nat. Phys.* **2023**, *19*, 201–209. [CrossRef]
2. Luo, L.; Yang, X.; Liu, X.; Liu, Z.; Vaswani, C.; Cheng, D.; Mootz, M.; Zhao, X.; Yao, Y.; Wang, C.Z.; et al. Ultrafast manipulation of topologically enhanced surface transport driven by mid-infrared and terahertz pulses in Bi_2Se_3. *Nat. Commun.* **2019**, *10*, 607. [CrossRef] [PubMed]
3. Luo, L.; Cheng, D.; Song, B.; Wang, L.L.; Vaswani, C.; Lozano, P.M.; Gu, G.; Huang, C.; Kim, R.H.J.; Liu, Z.; et al. A light-induced phononic symmetry switch and giant dissipationless topological photocurrent in $ZrTe_5$. *Nat. Mater.* **2021**, *20*, 329–334. [CrossRef] [PubMed]
4. Arnold, F.; Shekhar, C.; Wu, S.C.; Sun, Y.; Dos Reis, R.D.; Kumar, N.; Naumann, M.; Ajeesh, M.O.; Schmidt, M.; Grushin, A.G.; et al. Negative magnetoresistance without well-defined chirality in the Weyl semimetal TaP. *Nat. Commun.* **2016**, *7*, 11615. [CrossRef] [PubMed]
5. Liang, S.; Lin, J.; Kushwaha, S.; Xing, J.; Ni, N.; Cava, R.J.; Ong, N.P. Experimental tests of the chiral anomaly magnetoresistance in the Dirac-Weyl semimetals Na_3Bi and GdPtBi. *Phys. Rev. X* **2018**, *8*, 031002. [CrossRef]
6. Levy, A.L.; Sushkov, A.B.; Liu, F.; Shen, B.; Ni, N.; Drew, H.D.; Jenkins, G.S. Optical evidence of the chiral magnetic anomaly in the Weyl semimetal TaAs. *Phys. Rev. B* **2020**, *101*, 125102. [CrossRef]
7. Jadidi, M.M.; Kargarian, M.; Mittendorff, M.; Aytac, Y.; Shen, B.; König-Otto, J.C.; Winnerl, S.; Ni, N.; Gaeta, A.L.; Murphy, T.E.; et al. Nonlinear optical control of chiral charge pumping in a topological Weyl semimetal. *Phys. Rev. B* **2020**, *102*, 245123. [CrossRef]
8. Yuan, X.; Zhang, C.; Zhang, Y.; Yan, Z.; Lyu, T.; Zhang, M.; Li, Z.; Song, C.; Zhao, M.; Leng, P.; et al. The discovery of dynamic chiral anomaly in a Weyl semimetal NbAs. *Nat. Commun.* **2020**, *11*, 1259. [CrossRef]
9. Stinson, H.T.; Sternbach, A.; Najera, O.; Jing, R.; Mcleod, A.S.; Slusar, T.V.; Mueller, A.; Anderegg, L.; Kim, H.T.; Rozenberg, M.; et al. Imaging the nanoscale phase separation in vanadium dioxide thin films at terahertz frequencies. *Nat. Commun.* **2018**, *9*, 3604. [CrossRef]
10. Cocker, T.L.; Peller, D.; Yu, P.; Repp, J.; Huber, R. Tracking the ultrafast motion of a single molecule by femtosecond orbital imaging. *Nature* **2016**, *539*, 263–267. [CrossRef]
11. Wang, L.; Xia, Y.; Ho, W. Atomic-scale quantum sensing based on the ultrafast coherence of an H2 molecule in an STM cavity. *Science* **2022**, *376*, 401–405. [CrossRef] [PubMed]
12. Chen, H.T.; Kersting, R.; Cho, G.C. Terahertz imaging with nanometer resolution. *Appl. Phys. Lett.* **2003**, *83*, 3009–3011. [CrossRef]
13. Von Ribbeck, H.G.; Brehm, M.; Van der Weide, D.; Winnerl, S.; Drachenko, O.; Helm, M.; Keilmann, F. Spectroscopic THz near-field microscope. *Opt. Express* **2008**, *16*, 3430–3438. [CrossRef] [PubMed]
14. Zhang, J.; Chen, X.; Mills, S.; Ciavatti, T.; Yao, Z.; Mescall, R.; Hu, H.; Semenenko, V.; Fei, Z.; Li, H.; et al. Terahertz Nanoimaging of Graphene. *ACS Photonics* **2018**, *5*, 2645–2651. [CrossRef]
15. Aghamiri, N.A.; Huth, F.; Huber, A.J.; Fali, A.; Hillenbrand, R.; Abate, Y. Hyperspectral time-domain terahertz nano-imaging. *Opt. Express* **2019**, *27*, 24231–24242. [CrossRef] [PubMed]
16. Moon, K.; Do, Y.; Park, H.; Kim, J.; Kang, H.; Lee, G.; Lim, J.H.; Kim, J.W.; Han, H. Computed terahertz near-field mapping of molecular resonances of lactose stereo-isomer impurities with sub-attomole sensitivity. *Sci. Rep.* **2019**, *9*, 16915. [CrossRef] [PubMed]
17. Pizzuto, A.; Castro-Camus, E.; Wilson, W.; Choi, W.; Li, X.; Mittleman, D.M. Nonlocal Time-Resolved Terahertz Spectroscopy in the Near Field. *ACS Photonics* **2021**, *8*, 2904–2911. [CrossRef]
18. Plankl, M.; Faria Junior, P.E.; Mooshammer, F.; Siday, T.; Zizlsperger, M.; Sandner, F.; Schiegl, F.; Maier, S.; Huber, M.A.; Gmitra, M.; et al. Subcycle contact-free nanoscopy of ultrafast interlayer transport in atomically thin heterostructures. *Nat. Photonics* **2021**, *15*, 594–600. [CrossRef]
19. Kim, R.H.J.; Huang, C.; Luan, Y.; Wang, L.L.; Liu, Z.; Park, J.M.; Luo, L.; Lozano, P.M.; Gu, G.; Turan, D.; et al. Terahertz Nano-Imaging of Electronic Strip Heterogeneity in a Dirac Semimetal. *ACS Photonics* **2021**, *8*, 1873–1880. [CrossRef]
20. Kim, R.H.J.; Pathak, A.K.; Park, J.M.; Imran, M.; Haeuser, S.; Fei, Z.; Mudryk, Y.; Koschny, T.; Wang, J. Nano-compositional imaging of the lanthanum silicide system at THz wavelengths. *Optics Express* **2023**, *32*, 2356–2363 . [CrossRef]
21. Kim, R.H.J.; Liu, Z.; Huang, C.; Park, J.M.; Haeuser, S.J.; Song, Z.; Yan, Y.; Yao, Y.; Luo, L.; Wang, J. Terahertz Nanoimaging of Perovskite Solar Cell Materials. *ACS Photonics* **2022**, *9*, 3550–3556. [CrossRef]
22. Kim, R.H.J.; Park, J.M.; Haeuser, S.; Huang, C.; Cheng, D.; Koschny, T.; Oh, J.; Kopas, C.; Cansizoglu, H.; Yadavalli, K.; et al. Visualizing heterogeneous dipole fields by terahertz light coupling in individual nano-junctions. *Commun. Phys.* **2023**, *6*, 147. [CrossRef]
23. Wehmeier, L.; Liu, M.; Park, S.; Jang, H.; Basov, D.; Homes, C.C.; Carr, G.L. Ultrabroadband Terahertz Near-Field Nanospectroscopy with a HgCdTe Detector. *ACS Photonics* **2023**, *10*, 4329–4339. [CrossRef] [PubMed]
24. Taghinejad, M.; Xia, C.; Hrton, M.; Lee, K.T.; Kim, A.S.; Li, Q.; Guzelturk, B.; Kalousek, R.; Xu, F.; Cai, W.; et al. Determining hot-carrier transport dynamics from terahertz emission. *Science* **2023**, *382*, 299–305. [CrossRef] [PubMed]
25. Yang, H.U.; Hebestreit, E.; Josberger, E.E.; Raschke, M.B. A cryogenic scattering-type scanning near-field optical microscope. *Rev. Sci. Instrum.* **2013**, *84*, 023701. [CrossRef] [PubMed]

26. Ni, G.; McLeod, d.A.; Sun, Z.; Wang, L.; Xiong, L.; Post, K.; Sunku, S.; Jiang, B.Y.; Hone, J.; Dean, C.R.; et al. Fundamental limits to graphene plasmonics. *Nature* **2018**, *557*, 530–533. [CrossRef] [PubMed]
27. Lin, K.T.; Komiyama, S.; Kim, S.; Kawamura, K.i.; Kajihara, Y. A high signal-to-noise ratio passive near-field microscope equipped with a helium-free cryostat. *Rev. Sci. Instrum.* **2017**, *88*, 013706. [CrossRef]
28. Dapolito, M.; Chen, X.; Li, C.; Tsuneto, M.; Zhang, S.; Du, X.; Liu, M.; Gozar, A. Scattering-type scanning near-field optical microscopy with Akiyama piezo-probes. *Appl. Phys. Lett.* **2022**, *120*, 013104. [CrossRef]
29. Zhao, W.; Li, H.; Xiao, X.; Jiang, Y.; Watanabe, K.; Taniguchi, T.; Zettl, A.; Wang, F. Nanoimaging of low-loss plasmonic waveguide modes in a graphene nanoribbon. *Nano Lett.* **2021**, *21*, 3106–3111. [CrossRef]
30. Lu, Q.; Bollinger, A.T.; He, X.; Sundling, R.; Bozovic, I.; Gozar, A. Surface Josephson plasma waves in a high-temperature superconductor. *Npj Quantum Mater.* **2020**, *5*, 69. [CrossRef]
31. Dapolito, M.; Tsuneto, M.; Zheng, W.; Wehmeier, L.; Xu, S.; Chen, X.; Sun, J.; Du, Z.; Shao, Y.; Jing, R.; et al. Infrared nano-imaging of Dirac magnetoexcitons in graphene. *Nat. Nanotechnol.* **2023**, *18*, 1409–1415. [CrossRef]
32. Kim, R.H.J.; Park, J.M.; Haeuser, S.J.; Luo, L.; Wang, J. A sub-2 Kelvin cryogenic magneto-terahertz scattering-type scanning near-field optical microscope (cm-THz-sSNOM). *Rev. Sci. Instrum.* **2023**, *94*, 043702. [CrossRef] [PubMed]
33. Vaswani, C.; Wang, L.L.; Mudiyanselage, D.H.; Li, Q.; Lozano, P.; Gu, G.; Cheng, D.; Song, B.; Luo, L.; Kim, R.H.; et al. Light-driven Raman coherence as a nonthermal route to ultrafast topology switching in a Dirac semimetal. *Phys. Rev. X* **2020**, *10*, 021013. [CrossRef]
34. Chen, J.; Badioli, M.; Alonso-González, P.; Thongrattanasiri, S.; Huth, F.; Osmond, J.; Spasenović, M.; Centeno, A.; Pesquera, A.; Godignon, P.; et al. Optical nano-imaging of gate-tunable graphene plasmons. *Nature* **2012**, *487*, 77–81. [CrossRef] [PubMed]
35. Weng, H.; Dai, X.; Fang, Z. Transition-metal pentatelluride $ZrTe_5$ and $HfTe_5$: A paradigm for large-gap quantum spin Hall insulators. *Phys. Rev. X* **2014**, *4*, 011002.
36. Manzoni, G.; Gragnaniello, L.; Autès, G.; Kuhn, T.; Sterzi, A.; Cilento, F.; Zacchigna, M.; Enenkel, V.; Vobornik, I.; Barba, L.; et al. Evidence for a strong topological insulator phase in $ZrTe_5$. *Phys. Rev. Lett.* **2016**, *117*, 237601. [CrossRef] [PubMed]
37. Xu, B.; Zhao, L.; Marsik, P.; Sheveleva, E.; Lyzwa, F.; Dai, Y.; Chen, G.; Qiu, X.; Bernhard, C. Temperature-driven topological phase transition and intermediate Dirac semimetal phase in $ZrTe_5$. *Phys. Rev. Lett.* **2018**, *121*, 187401. [CrossRef]
38. Tang, F.; Ren, Y.; Wang, P.; Zhong, R.; Schneeloch, J.; Yang, S.A.; Yang, K.; Lee, P.A.; Gu, G.; Qiao, Z.; et al. Three-dimensional quantum Hall effect and metal–insulator transition in $ZrTe_5$. *Nature* **2019**, *569*, 537–541. [CrossRef]
39. Mutch, J.; Chen, W.C.; Went, P.; Qian, T.; Wilson, I.Z.; Andreev, A.; Chen, C.C.; Chu, J.H. Evidence for a strain-tuned topological phase transition in $ZrTe_5$. *Sci. Adv.* **2019**, *5*, eaav9771. [CrossRef]
40. Jing, R.; Shao, Y.; Fei, Z.; Lo, C.F.B.; Vitalone, R.A.; Ruta, F.L.; Staunton, J.; Zheng, W.J.C.; Mcleod, A.S.; Sun, Z.; et al. Terahertz response of monolayer and few-layer WTe_2 at the nanoscale. *Nat. Commun.* **2021**, *12*, 5594. [CrossRef]
41. Klarskov, P.; Kim, H.; Colvin, V.L.; Mittleman, D.M. Nanoscale laser terahertz emission microscopy. *ACS Photonics* **2017**, *4*, 2676–2680. [CrossRef]
42. Xu, S.; Li, Y.; Vitalone, R.A.; Jing, R.; Sternbach, A.J.; Zhang, S.; Ingham, J.; Delor, M.; McIver, J.; Yankowitz, M.; et al. Electronic interactions in Dirac fluids visualized by nano-terahertz spacetime mapping. *arXiv* **2023**, arXiv:2311.11502.
43. Maissen, C.; Chen, S.; Nikulina, E.; Govyadinov, A.; Hillenbrand, R. Probes for ultrasensitive THz nanoscopy. *ACS Photonics* **2019**, *6*, 1279–1288. [CrossRef]
44. Sobel, I.; Feldman, G. An isotropic 3x3 image gradient operator. *Present. Stanf. AI Proj.* **2014**, *1968*, 3.
45. Kittler, J. On the accuracy of the Sobel edge detector. *Image Vis. Comput.* **1983**, *1*, 37–42. [CrossRef]